Crystal, electronic structures and photoluminescence properties of rare-earth doped LiSi$_2$N$_3$

Y.Q. Li [a,b,*], N. Hirosaki [a], R.J. Xie [a], T. Takeka [a], M. Mitomo [a]

[a] Nitride Particle Group, Nano Ceramics Center, National Institute for Materials Science, Namiki 1-1, Tsukuba, Ibaraki 305-0044, Japan
[b] College of Materials Science and Engineering, Nanjing University of Technology, New Model Road 5, Nanjing, Jiangsu 210009, China

ARTICLE INFO

ABSTRACT

The crystal and electronic structures, and luminescence properties of Eu^{2+}, Ce^{3+} and Tb^{3+} activated LiSi$_2$N$_3$ are reported. LiSi$_2$N$_3$ is an insulator with an indirect band gap of about 5.0 eV (experimental value ~6.4 eV) and the Li 2s, 2p states are positioned on the top of the valence band close to the Fermi level and the bottom of the conduction band. The solubility of Eu^{2+} is significantly higher than Ce^{3+} and Tb^{3+} in LiSi$_2$N$_3$ which may be strongly related to the valence difference between Li$^+$ and rare-earth ions. LiSi$_2$N$_3$:Eu^{2+} shows yellow emission at about 580 nm due to the $4f^65d^1 \rightarrow 4f^7$ transition of Eu^{2+}. Double substitution is found to be the effective ways to improve the luminescence efficiency of LiSi$_2$N$_3$:Eu^{2+}, especially for the partial replacement of (LiSi)$^{5+}$ with (CaAl)$^{5+}$, which gives red emission at 620 nm, showing highly promising applications in white LEDs. LiSi$_2$N$_3$:Ce^{3+} emits blue light at about 450 nm arising from the $5d^1 \rightarrow 4f^15d^0$ transition of Ce^{3+} upon excitation at 320 nm. LiSi$_2$N$_3$:Tb^{3+} gives strong green line emission with a maximum peak at about 542 nm attributed to the $^5D_4 \rightarrow ^7F_J$ ($J = 3$–6) transition of Tb^{3+}, which is caused by highly efficient energy transfer from the LiSi$_2$N$_3$ host to the Tb^{3+} ions.

1. Introduction

Since the absorption of nitride based phosphors perfectly match with the radiation of the blue- and UV–LED chips, rare earth activated silicon nitride based materials have emerged as the best wavelength conversion phosphors for white-light LED applications [1,2]. The composition of nitride phosphors is normally focused on the alkaline earth silicon nitride/oxynitride, e.g., M$_2$Si$_5$N$_8$ [3–5] and MSi$_2$N$_2$O$_2$ [6] (M = Ca, Sr, Ba), as well as alkaline earth aluminum–silicon nitride/oxynitride, e.g., CaAlSiN$_3$ [7,8] or Ca-α-Sialon [9,10] etc., because the ionic size of M and/or its crystallographic size in the host lattice are suitable for the occupation of the rare-earth ions, i.e., Eu^{2+} and Ce^{3+} [11]. Additionally, a rigid lattice and high covalent environment around the rare-earth ions also play an important role for lowering the 5d excitation energy levels of Eu^{2+} and Ce^{3+} in nitrogen-rich lattice [12].

In some hosts the monovalent metal ion is significantly small like Li$^+$ in Li-a-Sialon [13] and even without the metal ion like in β-Sialon [14,15], however, Eu^{2+}-doped Li-α-Sialon and β-Sialon can also give very efficient greenish-yellow (~570 nm) and green (~530 nm) emission, respectively, under excitation in the spectral region of 375–450 nm. Both of them have been used as wavelength conversion phosphors for white LED applications. Therefore, in the course of searching for novel nitride based phosphors, it is necessary to study on unexplored compositional regions beyond the traditional phosphor materials. Ternary lithium silicon nitrides are one of such interesting hosts for use as luminescent materials. Among Li$_3$N–Si$_3$N$_4$ system, there are several ternary compounds, e.g., LiSi$_2$N$_3$ [16–20], Li$_2$SiN$_2$ [16,19,22,23], Li$_5$SiN$_3$ [16,19,21,24], Li$_{18}$Si$_3$N$_{10}$ [19], Li$_{21}$Si$_3$N$_{11}$ [19] and Li$_8$SiN$_4$ [16,19,21]. Despite some of them are still ambiguous in the crystal structures, the Li$^+$ ion conductivity of lithium silicon nitride compounds evidently shows an increased tendency corresponding to an increase in the Li/Si ratio [19,25]. Since the lithium ions can move rapidly within the framework of silicon nitride formed by corner-sharing of the tetrahedral SiN$_4$, these materials have shown high potential for solid state electrolytes in lithium battery applications [19,21,23,24,26]. Among above mentioned lithium silicon nitrides, LiSi$_2$N$_3$ is the most stable compound with a well-defined crystal structure, which is isostructural with Si$_2$N$_2$O and Li$_2$SiO$_3$ having wurizite-type structure (space group Cmc2$_1$) [18,20]. Similar to Si$_2$N$_2$O, the framework of [Si$_2$N$_3$]$^-$ in LiSi$_2$N$_3$ is built up by two-dimensional infinite, parallel layers of condensed [Si$_6$N$_6$] twelve-membered rings formed by corner sharing of the nitrogen atoms of the

* Corresponding author at: Nitride Particle Group, Nano Ceramics Center, National Institute for Materials Science, Namiki 1-1, Tsukuba, Ibaraki 305-0044, Japan. Fax: +81 29 851 3613.
E-mail address: li.yuanqiang@nims.go.jp (Y.Q. Li).

SiN_4 tetrahedra [20]. Li^+ occupies the 4a site and directly connects with four or five nitrogen atoms within the unit cell ($\sim$2.3 Å) or cross over unit cell ($\sim$2.7 Å), respectively. The most interesting point is that $LiSi_2N_3$ provides a nice structure, in which the nearest Li^+–Li^+ distance is just about 2.8 Å (slightly larger than the diameter of Eu^{2+} (2.34 Å) for coordination number CN = 6).

So far we could not find detailed reports on the luminescence properties of rare-earth doped lithium silicon nitride. Therefore, in the present work, undoped and rare-earth (Eu^{2+}, Ce^{3+} and Tb^{3+}) doped $LiSi_2N_3$ as well as its modifications materials using double substitution approaches were synthesized by a solid state reaction. The crystal structure in particular the local structures (the first nearest nitrogen atoms coordinated with the Li atom) are determined by the Rietveld refinement of powder X-ray diffraction. Furthermore, the electronic structures of $LiSi_2N_3$ are obtained by first principles calculations for a better understanding of the optical properties. Finally, the luminescence properties of Eu^{2+}, Ce^{3+} and Tb^{3+}-doped $LiSi_2N_3$ are present with a focus on the relationship between the crystal structure and the luminescence properties.

2. Experimental

2.1. Binary rare-earth nitrides

Binary rare-earth nitride compounds, EuN and CeN, were synthesized by a nitridation reaction of small metal pieces of Eu (Shin-Etsu Chemical Co., Ltd., purity 99%) and Ce (Shin-Etsu Chemical Co., Ltd., purity 99%) with high purity nitrogen (99.999%) at 800 °C for 16 h in a Mo boat within a horizontal tube furnace. The obtained rare-earth nitrides were determined to be approximately $EuN_{0.93}$ and $CeN_{0.96}$ by the weight-gain method. Powder X-ray powder diffraction (XRD) confirmed that the obtained $EuN_{0.93}$ and $CeN_{0.96}$ are in good agreement with the references of EuN (JCPDS 15-0087) and CeN (JCPDS 15-0882) both having cubic crystalline phase (Fm3m) with only traces of oxynitride-like secondary phases.

2.2. Undoped and rare-earth doped $LiSi_2N_3$

The compositions of $Li_{1-2x}Eu_xSi_2N_3$ ($x = 0$–0.02), $Li_{1-2x-y}Ca_yEu_xSi_{2-y}Al_yN_3$ ($x = 0.01$ and $y = 0$–0.04), $Li_{1-3x}Ce_xSi_2N_3$ ($x = 0.005$), and $Li_{1-3x}Tb_xSi_2N_{2.994167}O_{0.00875}$ ($x = 0.005$) were prepared by a solid state reaction using Li_3N (Aldrich, purity 99%), α-Si_3N_4 (UBE, SN-E10, α content $\sim$93%), Ca_3N_2 (Shin-Etsu Chemical Co., Ltd., purity > 99%), and AlN (Tokuyama, F-grade) as well as $EuN_{0.93}$, $CeN_{0.96}$ and Tb_4O_7 (Shin-Etsu Chemical Co., Ltd., purity > 99.9%) as the starting materials. In the case of $Li_{1-2x}Eu_xSi_{2-y}Al_yN_{3-y}O_y$ ($x = 0.01$, $y = 0.04$), Eu_2O_3 (Shin-Etsu Chemical Co., Ltd., purity > 99.99%) was used as the sources of both oxygen and Eu instead of $EuN_{0.93}$. The appropriate amounts of the starting powders were mixed in stoichiometric compositions and ground in an agate mortar. The well-mixed powders were switched to a Mo crucible and then transferred into a tightly closed alumina tube. All the processes were carried out in a nitrogen-filled glove box. Subsequently, the samples were fired at 1400 °C for 6 h under N_2–H_2 (5%) atmosphere in a horizontal tube furnace for twice at the same conditions. To prevent the evaporation of lithium, the cap of the Mo crucible was tightly closed during the firing.

2.3. Characterization

The phase formation and crystal structure of all the samples were determined by the powder X-ray diffraction (Rigaku, RINT Ultima-III) with graphite monochromator using Cu-$K\alpha$ radiation operating at 40 kV and 40 mA. For structure determination, the XRD data were collected in the 2θ range of 10°–120° by a step scan mode (step size: 0.02; count time: 10 s per step). The Rietveld refinement was performed by the GSAS package [27,28] using the single crystal data [20] as an initial model.

The photoluminescence spectra were recorded by a fluorescence spectrophotometer (Hitachi, F-4500) at room temperature. The excitation and emission slits were fixed at 0.25 nm and the scan speed was set to 240 nm/min. The diffuse reflection spectrum was measured by a UV/Vis spectrophotometer (JASCO, V-560) with a $BaSO_4$ white plate as a standard reference. The temperature dependent luminescence was recorded on an intensified multi-channel spectrophotometer (Otsuka Electronics, MCPD-7000) with a 200 W Xe-lamp as an excitation source under excitation at 310 nm from room temperature to 200 °C by a heating rate of 100 °C/min. The holding time is fixed at about 5 min for each temperature point.

2.4. Computational procedure

The electronic structures of the $LiSi_2N_3$ host were calculated using the first principles plane wave-basis pseudopotential method [29] within the density functional theory performed by the VASP code [30–32] on the basis of a single crystal structural model [20]. The projector augmented wave pseudopotentials were adapted for Li, Si and N atoms. Exchange-correlation were treated with the generalized gradient approximation (GGA) using a Perdew-91 functional form [33]. The numerical integration of the Brillouin zone (BZ) was performed using a discrete $8 \times 8 \times 12$ Monkhorst-Pack k-point sampling and the plane-wave cutoff energy was set to be 500 eV. In order to study the chemical bonding situations of Li–N and Li–Li, the crystal orbital Hamiltonian population (COHP) [34] was also calculated self-consistently using the scalar-relativistic TB-LMTO-ASA method [35]. Density-functional theory (DFT) is employed with the local-density-approximation (LDA) exchange-correlation potential [36] and a $12 \times 12 \times 8$ k-mesh in the full Brillouin zone.

3. Results and discussion

3.1. Electronic structures of $LiSi_2N_3$

Fig. 1 shows the atomic projected density of states (DOS) for the Li, Si and N atoms, as well as the total density of states for $LiSi_2N_3$. The valence band is mainly composed of Li 2s, 2p, Si 3s, 3p and N 2p states ranging from −9 eV to the Fermi level (E_f), in which the Si 3p are largely hybridized with the N 2p states from −8 to 0 eV. The bandwidth of the 2p states of N (N1[3], N2[2]) and the 3p states of Si are about 9 eV, close to that in Si_3N_4 ($\sim$10 eV [37]). The N 2s and Si 3s along with the partial 3p states lie in lower energy regions below −13.5 eV having an energy gap of 4.2 eV with the top of the valence bands. The N 2p and Li 2p states are mainly hybridized at the upper part of the valence band from −2.5 eV to the Fermi level. Therefore, the formation of chemical bonds between the Li 2p and N 2p orbitals as well as the Si 3p and N 2p states was found in $LiSi_2N_3$. Unlike other metal silicon nitrides, such as $MgSiN_2$ [38], $BaSi_7N_{10}$ [39], $M_2Si_5N_8$ (M = Ca, Sr, Ba) [40] and $Ba_5Si_2N_6$ [41], where the partial DOS of the s and p states of the metal ions, namely Mg, Ca, Sr and Ba, are almost empty close to the Fermi level or far away from the Fermi level deeply lower-lying in the valence band. The 2s and 2p states of Li, however, are located at both valence and conduction bands.
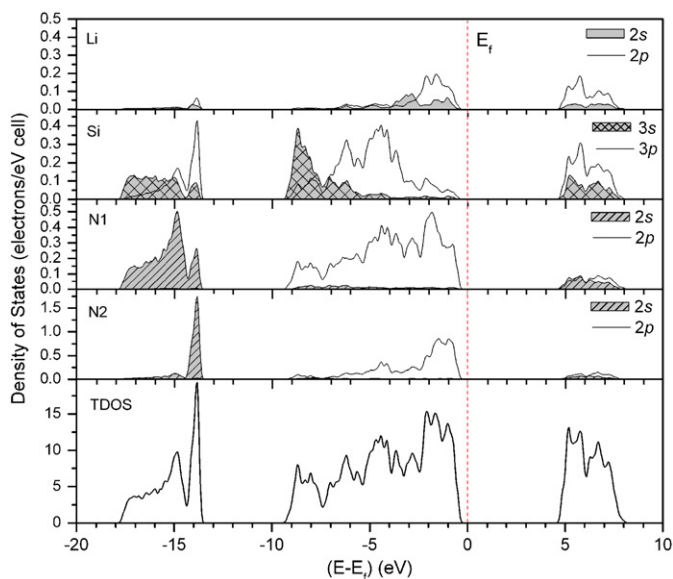
Fig. 1. Total and partial (Li, Si, N atoms) density of states of LiSi$_2$N$_3$. The Fermi level is set at zero energy.

Fig. 2. Band structure of LiSi$_2$N$_3$. The indirect band gap is about 5.0 eV between Γ (CB) and Γ–Z (VB).

Especially, the Li 2p and 2s states are relatively strong and positioned at higher energies just below the Fermi level and mainly distributed from -5 to 0 eV (Fig. 1). The bottom of the conduction bands is mainly composed of Si 3p, 3s and Li 2p as well as N1 3s, 3p states. Fig. 2 depicts the band structure of LiSi$_2$N$_3$ along high symmetry points of the irreducible Brillouin zone. It is clear that the top of the valence band is within the Γ–Z region and the bottom of the conduction band is at the Γ point. The indirect band gap between the valence and conduction bands is estimated to be about 5.0 eV and a direct band gap at Γ is about 5.6 eV, demonstrating that LiSi$_2$N$_3$ is an insulator material. The calculated band gap is in fair agreement with the experimental optical band gap of about 6.4 eV, which was determined by the diffuse reflection spectrum of undoped LiSi$_2$N$_3$ powder (see section below). A large difference between the calculated and experimental value in the band gaps is probably attributed to two reasons. Firstly, the DFT approximation (GGA) normally cannot correctly deal with and always underestimates the band gaps; secondly, the fundamental absorption edge of the prepared LiSi$_2$N$_3$ powder is located in the range of 200–230 nm which is already within lower-limit of our UV/Vis machine, therefore, additional errors also could be resulted from that.

The chemical bonding interactions of COHP for Li–N and Li–Li combined with the Li project DOS are plotted in Fig. 3. The lower-lying bands below the Fermi level are proved to be Li–N bonding between -10 eV and the Fermi energy level (E$_f$), whereas the higher-lying bands above 5 eV are Li–N antibonding. As expected, the chemical bonding of Li–Li shows strongly antibonding characteristic in the conduction band (Fig. 3). It should be noted that slight differences between the partial DOS of Li is ascribed to the different approximations of VASP and LMTO–ASA. From the above calculations, we might conclude that the 2p electrons of Li close to the Fermi energy level would be easily promoted to the high energy levels (i.e., impurity levels) even to the conduction band by the radiation energy although there is a large energy gap in LiSi$_2$N$_3$. If so, as a consequence, a number of holes would leave at the Li site in the valence band. In addition, strong antibonding behavior of Li–Li implies that the solubility of the rare-earth ions would be very limited in LiSi$_2$N$_3$, which well agrees with our observations (see sections below).
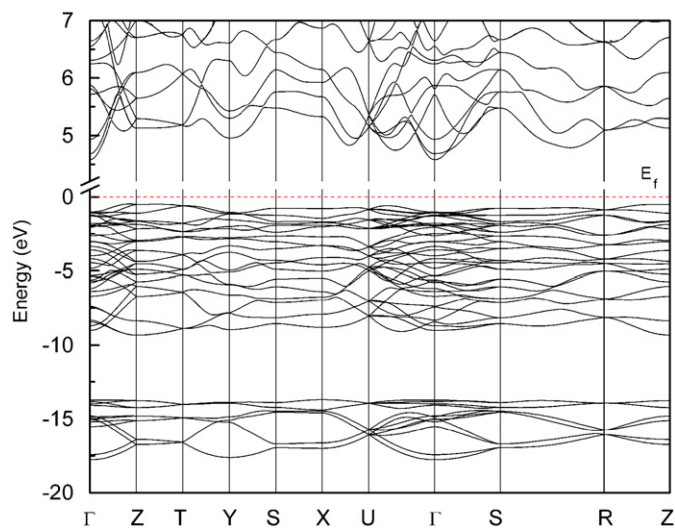
3.2. Structural characteristics of Eu^{2+}, Ce^{3+} and Tb^{3+} in LiSi$_2$N$_3$

As we mentioned before, it is interesting to know if or how much rare-earth ions can be incorporated into a significant small crystallographic site of Li$^+$ in LiSi$_2$N$_3$ in order to understand the interactions between Eu^{2+}–Eu^{2+}, Ce^{3+}–Ce^{3+} and Tb^{3+}–Tb^{3+}. With decreasing the ionic radius of the rare-earth ions going from Eu^{2+} (1.17 Å, CN = 6), via Ce^{3+} (1.01 Å, CN = 6) to Tb^{3+} (0.92 Å, CN = 6) [42], surprisingly, the solubility of small ionic size of Ce^{3+} and Tb^{3+} is significantly lower than that of large Eu^{2+}. The maximum solubility of Ce^{3+} and Tb^{3+} should be lower than 0.5 mol% with respect to Li$^+$ because even at 0.5 mol% ($x = 0.005$) in Li$_{1-3x}$Ln$_x$Si$_2$N$_3$ (Ln = Ce, Tb), a small amount of unidentified second phases ($<1.5\%$) can be observed from their X-ray diffraction patterns. As a typical example, the Rietveld refinement powder X-ray diffraction pattern of Tb^{3+} doped LiSi$_2$N$_3$ is shown in Fig. 4a, in which the marked peaks indicate the impurity phases. Therefore, a large difference in valence between Li$^+$ and Ce^{3+} or Tb^{3+} may be a major reason although Ce^{3+} or Tb^{3+} has a smaller ionic size than that of Eu^{2+}. In contrast, a large amount of Eu^{2+} can be incorporated into the host lattice and can form the single phase solid solution of Li$_{1-2x}$Eu$_x$Si$_2$N$_3$, evidently showing by the serial XRD patterns of Li$_{1-2x}$Eu$_x$Si$_2$N$_3$ (Fig. 5a) and the Rietveld refinement XRD pattern of Li$_{1-2x}$Eu$_x$Si$_2$N$_3$ ($x = 0.005$) in Fig. 4b. Since significantly low luminescence efficiency for $x > 0.02$, further work beyond this range was not performed, however, the maximum solubility of Eu^{2+} is estimated to be at least greater than $x = 0.02$ for Li$_{1-2x}$Eu$_x$Si$_2$N$_3$. Fig. 5b depicts the variation of the lattice parameters of Li$_{1-2x}$Eu$_x$Si$_2$N$_3$ ($x = 0$–0.02) with an increase in Eu^{2+} concentration. The total lattice volume change is just about 0.2% from $x = 0$ to 0.02 (Fig. 5c), corresponding to the limited increases of the a, b, and c axes in total (Fig. 5b). Therefore, it seems that Eu^{2+} is nearly sunk in LiSi$_2$N$_3$ because it is generally expected that the replacement of Li$^+$ with Eu^{2+} will result in a large expansion of the host lattice. This unusual behavior may be caused by the aliovalent replacement of Li$^+$ with Eu^{2+}, which can be formulated as Li$_{1-2x}$Eu$_x$V$_{Li}$Si$_2$N$_3$. Thus, the formation of Li vacancies (i.e., V$_{Li}$) resulting in some extent shrinkage probably counterparts the overall expansion of the lattice volume arising from the Eu^{2+} ions incorporation. It also seems that the valence
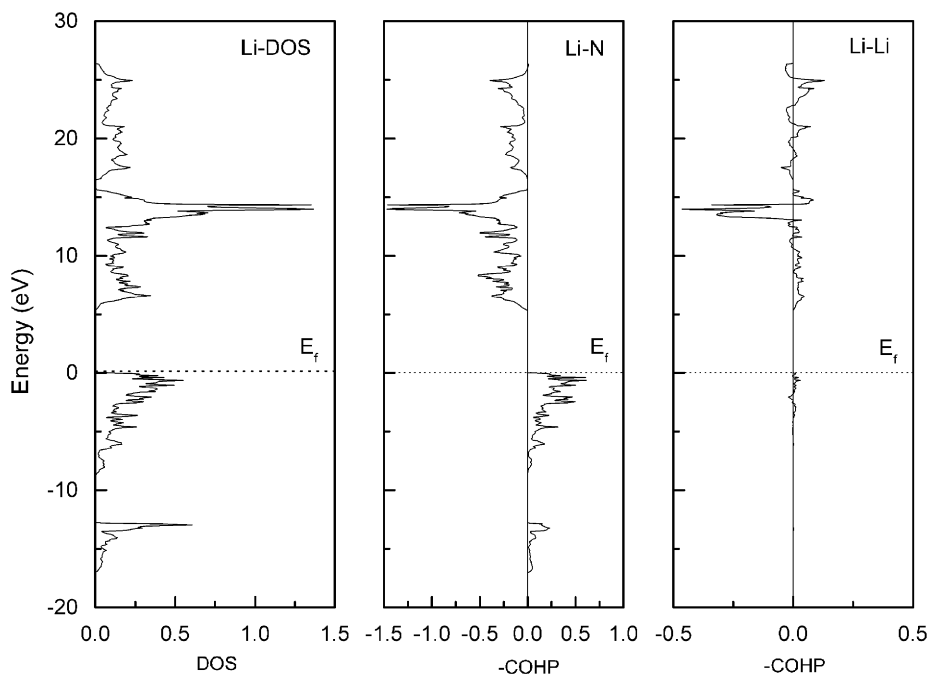
Fig. 3. Projected density of states of Li and the COHP for Li–N and Li–Li interactions by the TB-LMTO-ASA method.
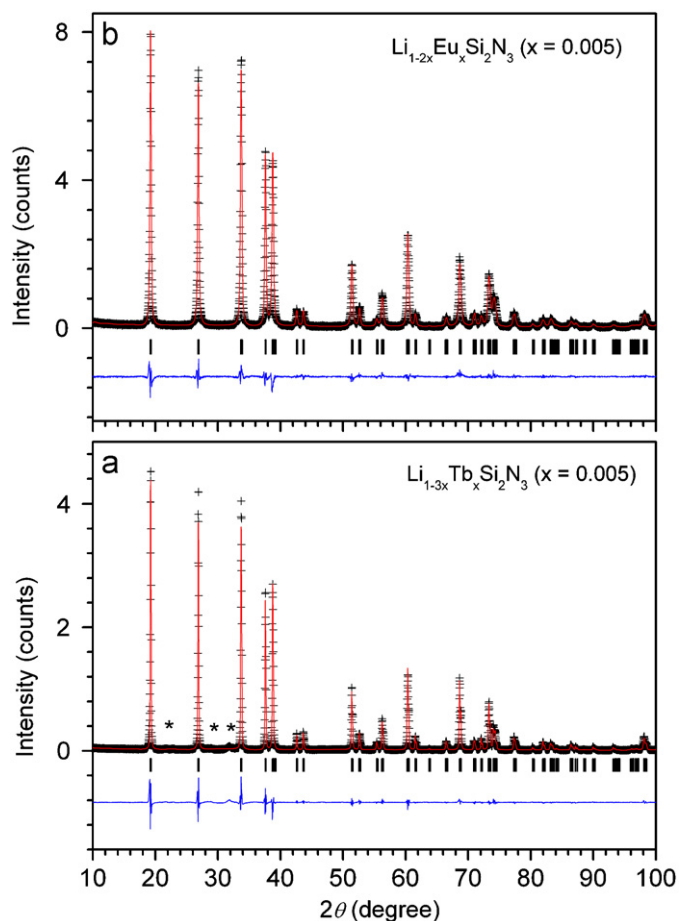

Fig. 4. Rietveld refinement powder X-ray diffraction patterns of Eu^{2+} and Tb^{3+} doped $LiSi_2N_3$. The vertical bars below the observed XRD pattern are the possible reflection lines of $LiSi_2N_3$. The starred peaks in Fig. 4a indicate the impurity phase in $LiSi_2N_3:Tb^{3+}$.

effect is more significant than the size effect in the formation of Eu, Ce, and Tb doped solid solution of $LiSi_2N_3$.

Within space group of $Cmc2_1$ at the 4a site, Li is directly coordinated by five nearest nitrogen atoms (3 $N^{[2]}$ and 2 $N^{[3]}$) in 2.7 Å, having the average Li–N distance of about 2.257 Å for $LiSi_2N_3$. Also it can be regarded as Li being connected with four N atoms in 2.3 Å, while concerning large rare-earth ions, it is believed that five-fold coordination with N is more suitable for Eu^{2+}, Ce^{3+} and Tb^{3+} based on the fact that the calculated coordination polyhedral volume [43] of LiN_4 is too small (∼4.957 Å^3) to accommodate the Eu^{2+}, Ce^{3+} and Tb^{3+} ions. Fig. 6 shows the crystal structure of $Li_{1−2x}Eu_xSi_2N_3$ ($x = 0.002$) and the local coordination of Li with N. Table 1 summarizes the crystallographic data for Eu^{2+}, Ce^{3+} and Tb^{3+}-doped $LiSi_2N_3$ and Table 2 gives the interatomic distances of Li–N, Si(Al)–N and Li–Li. In comparison with the overall lattice volume, the changes of the local coordination around Li^+ are slightly profound which increase about 3% and 0.5% from $x = 0$ to 0.02 for the coordination polyhedral volume of $Li_{Eu}N_5$ and the average Li_{Eu}–N distance, respectively (Fig. 7). The nearest distance of Li_{Eu}–Li_{Eu} ranges from 2.797 to 2.865 Å, and no obviously systematic changes can be found with increasing Eu^{2+} concentration. The average Si–N distance, however, slightly decreases with an increase in Eu^{2+} concentration from 1.739 to 1.733 Å with varying x from 0 to 0.02 in $Li_{1−2x}Eu_xSi_2N_3$. Corresponding to a unit cell volume decrease, going from Eu via Tb to Ce doped $LiSi_2N_3$, the nearest distances of Li–Li is decreased (Table 2). This trend is also applied to $Li_{1−2x−y}Ca_yEu_xSi_{2−y}Al_yN_3$ ($x = 0.01$ and $y = 0.04$). Interestingly, the average Si–N distance shows an increase trend in reversed to the change of Li–Li (Table 2).

In order to understand the influences of the composition/local structure (e.g. interatomic distances of Li_{Eu}–N as well as Li_{Eu}–Li_{Eu}) on the luminescence properties of $LiSi_2N_3:Eu^{2+}$, two double substitution approaches have been performed, that are $(AlO)^+$ substitution for $(SiN)^+$ and $(CaAl)^{5+}$ substitution for $(LiSi)^{5+}$. It is very common for the first but unusual for the second routine. Here, we focus on the substitution $(CaAl)^{5+}$ for $(LiSi)^{5+}$,

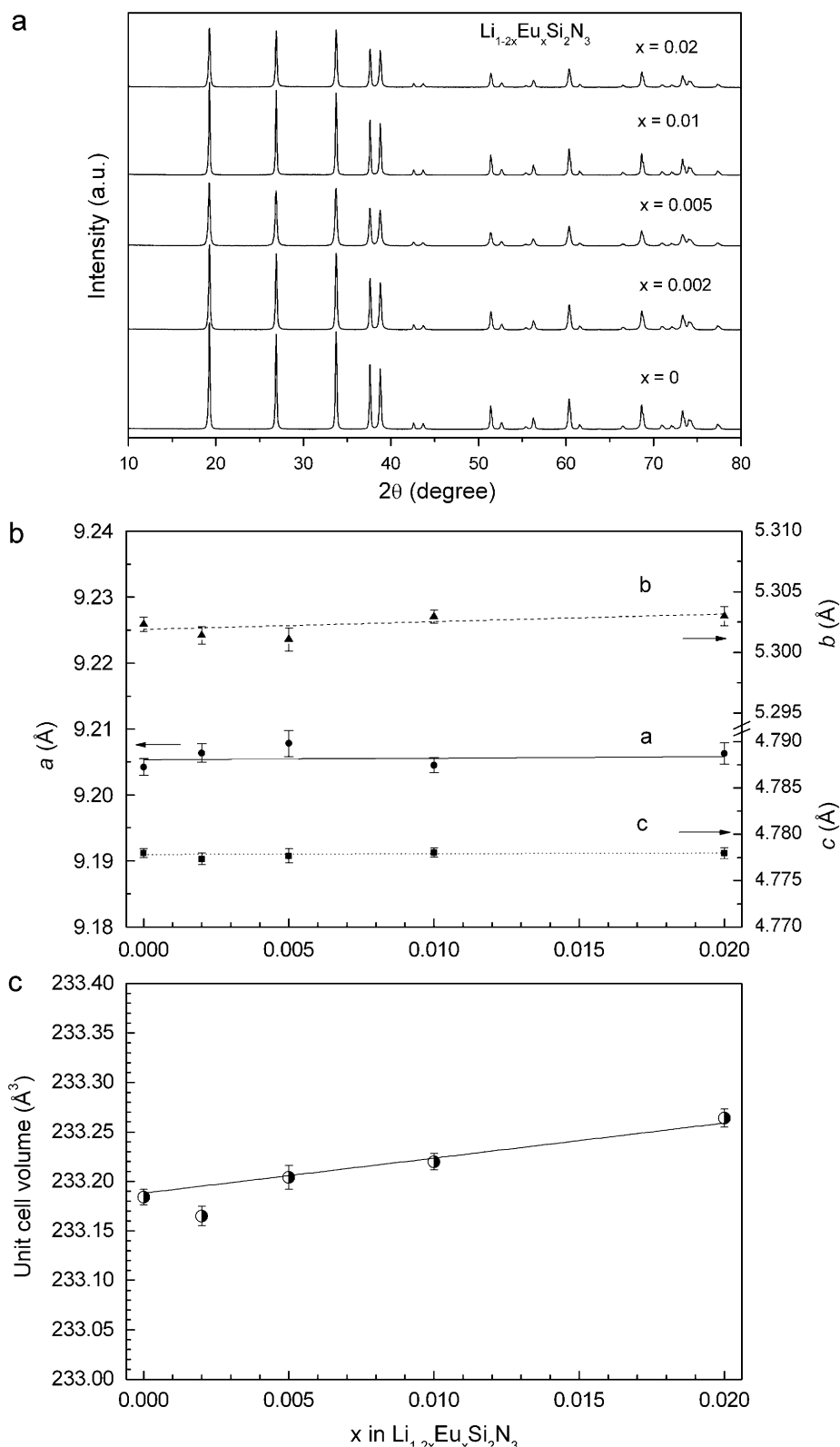**Fig. 5.** The powder X-ray diffraction patterns of $Li_{1-2x}Eu_xSi_2N_3$ ($x = 0$–0.02) (a), the lattice parameters a, b and c (b), and the unit cell volume (c) as a function of x.

viz. $Ca^{2+} \rightarrow Li^+$ and $Al^{3+} \rightarrow Si^{4+}$ simultaneously, as the luminescence properties of LiS_2N_3:Eu^{2+} can be significantly modified by this way (see next section). Fig. 8 illustrates the Rietveld refinement XRD pattern of $Li_{1-2x-y}Ca_yEu_xSi_{2-y}Al_yN_3$ ($x = 0.01$ and $y = 0.04$), indicating that a limited solid solution can be realized by this substitution. Unfortunately, the maximum solubility is just at around $y = 0.04$, and for higher y values the secondary phase like α-Si_3N_4 or α-Sialon has been appeared under the present synthetic conditions. If higher solubility of $(CaAl)^{5+}$ could be reached, the structure/composition would be going to $CaAlSiN_3$ [7–8] as expected. Due to large $(CaAl)^{5+}$ pair replacement of small $(LiSi)^{5+}$ pair, the lattice parameters ($a = 9.2204(5)\,Å$, $b = 5.3107(2)$
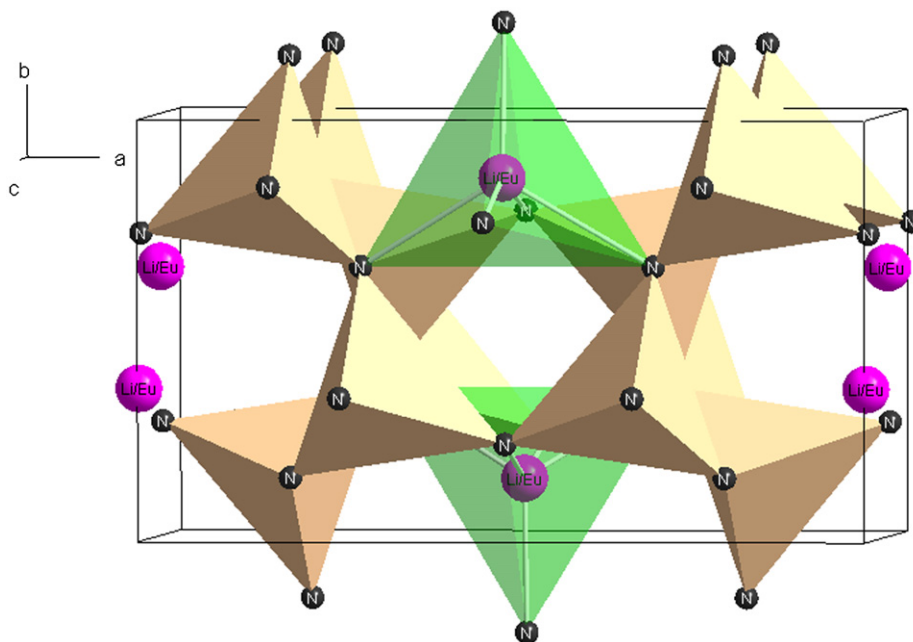
**Fig. 6.** Projection of the crystal structure and the local coordination of Li_{Eu} with nitrogen atoms in $Li_{1-2x}Eu_xSi_2N_3$ ($x = 0.002$).

Table 1
Crystal structure data and isotropic displacement parameters for Eu^{2+}, Ce^{3+} and Tb^{3+} doped $LiSi_2N_3$ and $Li_{1-2x-y}Ca_yEu_xSi_{2-y}Al_yN_3$ ($x = 0.01$ and $y = 0.04$).

Crystal system: Orthorhombic; Space group: Cmc21(36); Z = 4						
Formula	$Li_{0.99}Eu_{0.005}Si_2N_3$					
Lattice parameters	$a = 9.2078(3)$, $b = 5.3011(2)$, $c = 4.7777(1)$, $V = 233.20(1)$					
R_{wp}	8.8%					
R_p	6.5%					
Atom	Wyck.	x/a	y/b	z/c	SOF	U (100 Å²)
(Li, Eu)1	4a	0.0000	0.3509(21)	−0.0458(21)	0.99/0.005	0.62(2)
Si1	8b	0.1665(2)	0.8347(3)	0.9769(5)	1.00	0.75(10)
N1	8b	0.2022(4)	0.8555(10)	0.3489(1)	1.00	0.56(2)
N2	4a	0.0000	0.2703(7)	0.4098(10)	1.00	0.52(6)
Formula	$Li_{0.985}Ce_{0.005}Si_2N_3$					
Lattice parameters	$a = 9.2064(2)$, $b = 5.3011(1)$, $c = 4.7770(1)$, $V = 233.14(1)$					
R_{wp}	10.5%					
R_p	7.5%					
(Li, Ce)1	4a	0.0000	0.3576(25)	−0.0389(33)	0.985/0.005	1.01(30)
Si1	8b	0.1667(2)	0.8358(3)	0.9815(1)	1.00	0.50(3)
N1	8b	0.2000(5)	0.8542(9)	0.3481(5)	1.00	0.26(13)
N2	4a	0.0000	0.2729(9)	0.4085(9)	1.00	0.02(1)
Formula	$Li_{0.985}Tb_{0.05}Si_2N_{2.9125}O_{0.0875}$					
Lattice parameters	$a = 9.2029(2)$, $b = 5.3031(1)$, $c = 4.7782(1)$, $V = 233.19(1)$					
R_{wp}	10.6%					
R_p	7.5%					
(Li, Tb)1	4a	0.0000	0.3530(28)	−0.0868(29)	0.985/0.005	2.26(1)
Si1	8b	0.1668(2)	0.8354(32)	0.9381(6)	1.00	0.71(6)
(N, O)1	8b	0.2006(5)	0.8552(10)	0.3050(1)	0.971/0.007	0.27(13)
(N, O)2	4a	0.0000	0.2700(9)	0.3669(12)	0.971/0.007	0.01(10)
Formula	$Li_{0.94}Ca_{0.04}Eu_{0.01}Al_{0.04}Si_{1.96}N_3$					
Lattice parameters	$a = 9.2204(5)$, $b = 5.3107(2)$, $c = 4.7861(1)$, $V = 234.36(2)$					
R_{wp}	9%					
R_p	6.7%					
(Li, Ca, Eu)1	4a	0.0000	0.3506(24)	−0.0445(19)	0.94/0.04/0.01	2.10(1)
(Si, Al)1	8b	0.1668(2)	0.8331(4)	0.9836(1)	0.98/0.02	0.68(4)
N1	8b	0.2025(5)	0.8603(13)	0.3542(1)	1.00	0.02(3)
N2	4a	0.0000	0.2657(8)	0.4209(10)	1.00	0.04(9)

*a, b and c in (Å); V in (Å³); SOF = site occupancy fraction.

Table 2
Selected interatomic distances of Li–N, Si(Al)–N and the nearest Li–Li distance for Eu^{2+}, Ce^{3+} and Tb^{3+} doped $LiSi_2N_3$ and $Li_{1-2x-y}Ca_yEu_xSi_{2-y}Al_yN_3$ ($x = 0.01$ and $y = 0.04$).

Distance	$Li_{0.99}Eu_{0.005}Si_2N_3$	$Li_{0.985}Ce_{0.005}Si_2N_3$	$Li_{0.985}Tb_{0.05}Si_2N_{2.9125}O_{0.0875}$	$Li_{0.94}Ca_{0.04}Eu_{0.01}Al_{0.04}Si_{1.96}N_3$
Li1–N1	2.217(7) × 2	2.223(8) × 2	2.212(9) × 2	2.231(7) × 2
Li1–N2	2.636(10)	2.677(15)	2.647(14)	2.598(10)
Li1–N2	2.218(10)	2.184(16)	2.212(13)	2.272(9)
Li1–N2	2.019(12)	1.975(13)	2.011(15)	2.044(13)
Mean	2.261	2.256	2.259	2.275
Li1–Li1[a]	2.865(12) × 2	2.826(14) × 2	2.853(16) × 2	2.871(14) × 2
Mean	2.865	2.826	2.853	2.871
Si1–N1[a]	1.811(3)	1.781(2)	1.784(3)	1.810(3)
Si1–N1	1.783(5)	1.789(5)	1.787(6)	1.773(7)
Si1–N1	1.689(5)	1.710(5)	1.708(6)	1.700(7)
Si1–N2	1.662(3)	1.676(3)	1.668(3)	1.653(3)
Mean	1.736	1.739	1.737	1.734

[a] For $Li_{0.94}Ca_{0.04}Eu_{0.01}Al_{0.04}Si_{1.96}N_3$, Li1 = (Li, Ca)1 and Si1 = (Si, Al)1.
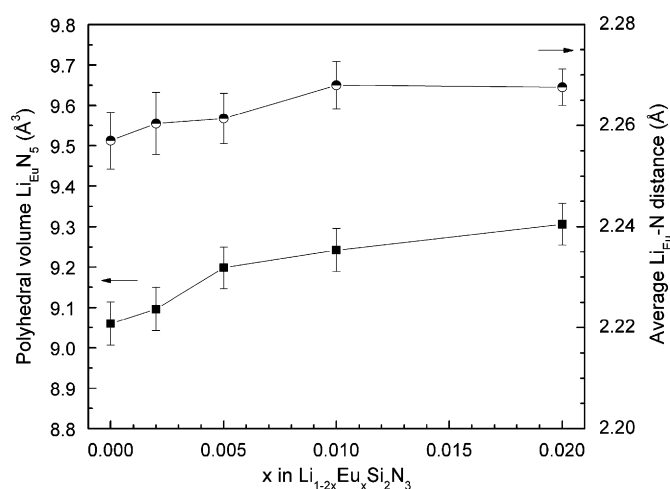
Fig. 7. Variation of the coordination polyhedral volume of $Li_{Eu}N_5$ and the average Li_{Eu}–N bond length with x of $Li_{1-2x}Eu_xSi_2N_3$.
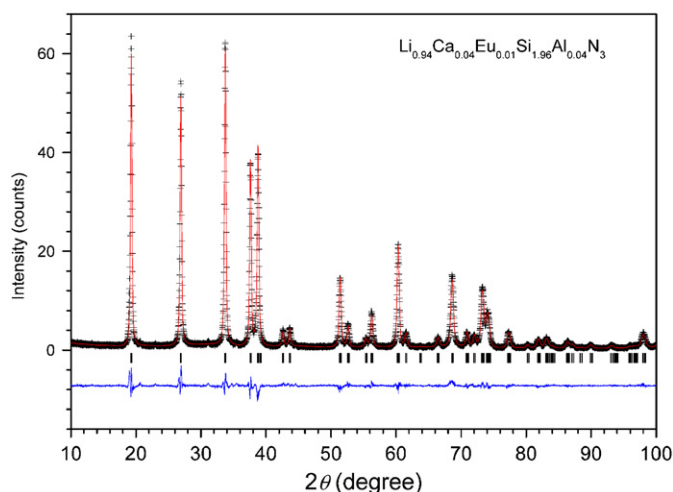
Fig. 8. Rietveld refinement powder X-ray diffraction patterns of $Li_{1-2x-y}Ca_yEu_xSi_{2-y}Al_yN_3$ ($x = 0.01$ and $y = 0.04$). The vertical bars below the observed XRD pattern are the possible reflection lines of $LiSi_2N_3$.

Å, $c = 4.7861(1)$ Å and $V = 234.363(16)$ Å^3) significantly increase in a, b and c as well as the unit cell volume (V) based on the fact that Al–N and Ca–N are longer than that of the Si–N and Li–N bond length [44,45]. As a consequence, the average bond length of $Li_{(Ca,Eu)}$–N and the coordination polyhedral volume of $Li_{(Ca,Eu)}N_5$ are increased to 2.2752 Å and 9.406 Å^3, respectively, in comparison with $Li_{0.98}Eu_{0.01}Si_2N_3$ (2.2680 Å and 9.242 Å^3, respectively). In the framework, as discussed before, the Si(Al)–N distance slightly decrease unexpectedly. With such large relaxations in the whole and local structures, thus a significant change in the luminescence of Eu^{2+} is understandable (see next section).

3.3. Photoluminescence properties

3.3.1. $LiSi_2N_3$:Eu^{2+}

Fig. 9a shows the excitation and emission spectra as a function of Eu^{2+} concentration. Similar to $CaAlSiN_3$:Eu^{2+}, the dominant excitation band of Eu^{2+} is also found at relative high energy peaking at about 310 nm, which probably associated with their small crystallographic site. Because the average bond length of Li_{Eu}–N (~ 2.26 Å) and the coordination polyhedral volume $Li_{Eu}N_5$ (~ 9.4 Å^3) are much smaller than that of M_{Eu}–N (M = Ca, Sr, Ba > 2.4 Å) and $M_{Eu}N_n$ ($n = 6$–8, > 15 Å^3), respectively, the 5d excitation states of Eu^{2+} are widely distributed from 210 to 500 nm in a number of alkaline earth silicon (aluminum) nitride compounds [3,4,8] with a low coordination number of CN = 5. Apparently, the excitation band seems to be composed of a single broad band at lower Eu concentrations, in particular for $x < 0.005$. However, this broad overlapping excitation band can be well decomposed into several Gaussian subbands centered approximately at 257, 298, 352 and 414 nm for $Li_{1-2x}Eu_xSi_2N_3$ ($x = 0.005$). Moreover, the longest excitation band can be further decomposed into two Gaussians at higher Eu concentrations. This is in good agreement with the observed excitation bands for high Eu concentration ($x \geqslant 0.01$), where the crystal field components of the Eu^{2+} 5d states are located at about 256, 307, 351, 403 and 444 nm for $x = 0.01$ and 0.02 (not shown in Fig. 9a). An excitation band in the range of 200–230 nm does not belong to Eu^{2+} but to the electrons transition from the valence to conduction bands of the $LiSi_2N_3$ host in agreement with its diffuse reflection spectrum (Fig. 9d). In addition, this band strongly overlaps with the upper 5d excitation bands of Eu^{2+} especially with the first two bands at about 257 and 298 nm, as shown in Fig. 9b. As discussed in Section 3.1, the calculated band gap is about 5.0 eV (experimental optical band gap ~ 6.4 eV) between the valence and conduction bands of
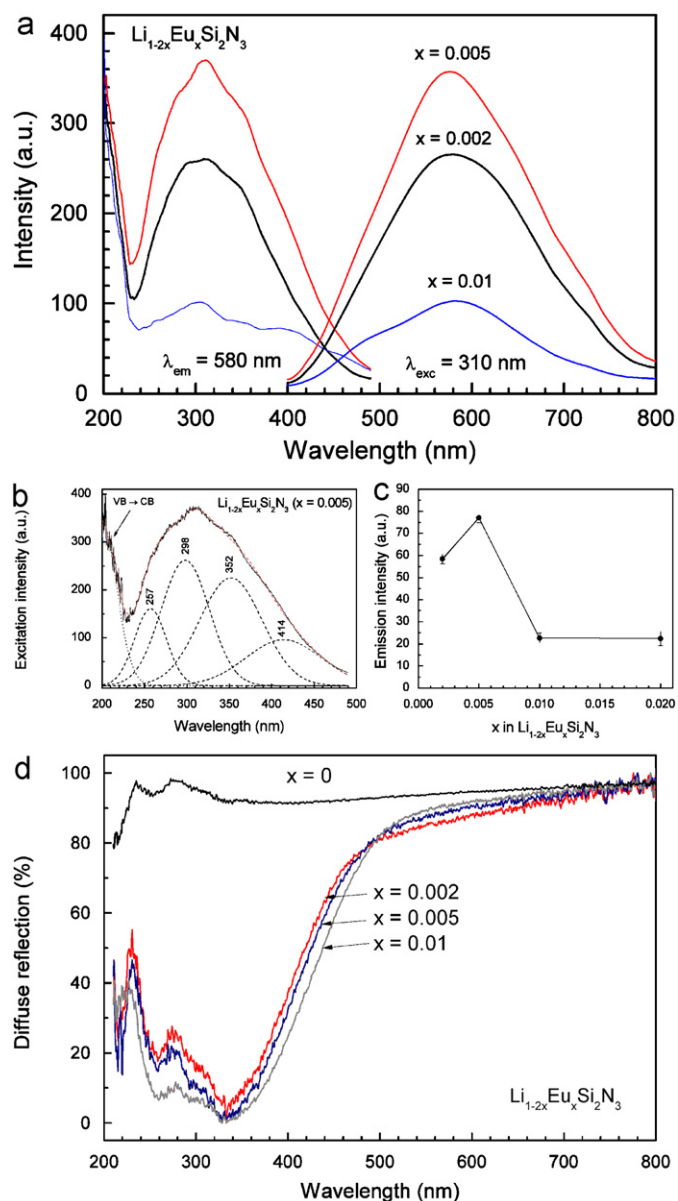
Fig. 9. Excitation and emission spectra of $Li_{1-2x}Eu_xSi_2N_3$ ($x = 0.002$–0.01) (a), the decomposed excitation bands with the Gaussian subbands for $x = 0.005$ (b), and the emission intensity as a function of x (c). The diffuse reflection spectra of $Li_{1-2x}Eu_xSi_2N_3$ ($x = 0$–0.01) (d).

$LiSi_2N_3$. In general, it needs high energy to promote the electrons in the occupied band to the unoccupied band with a large energy gap. However, Li $2p$ and/or $2s$ electrons can be easily promoted to the conduction band by means of the intermediate $5d$ levels of Eu^{2+} by lower radiation energies in $Li_{1-2x}Eu_xSi_2N_3$. This can be explained by two effects. Firstly, the Li $2p$ state within the top of the valence bands is very close to the Fermi level and has comparable intensity as that in the bottom of the conduction bands, as shown in the project DOS of the Li atom in Fig. 1. Secondly, the lowest $5d$ excited energy levels of Eu^{2+} or Ce^{3+} (see Section 3.3.2) are normally at very low energy particularly in nitride lattices. For example, the lowest $5d$ excited level of Eu^{2+} is at about 2.99 eV in $Li_{1-2x}Eu_xSi_2N_3$ ($x = 0.005$).

$LiSi_2N_3$:Eu^{2+} exhibits greenish-yellow emission with an asymmetry broad band peaking at about 572–584 nm, depending on the Eu concentration. Apart from the main emission band of Eu^{2+}, a shoulder at about 480 nm is also observed especially at higher

Eu^{2+} concentrations. On the basis of the fact that only one crystallographic site of Li is available in the $LiSi_2N_3$ lattice, a single emission band of Eu^{2+} is expected to be observed. Therefore, this shoulder may be attributed to the band to band emission, namely the electron transition from the conduction to valence bands of the host lattice. With increasing Eu concentration, the emission intensity increases up to $x = 0.005$ and then remarkably decreases for $x > 0.005$ in $Li_{1-2x}Eu_xSi_2N_3$ due to significant concentration quenching of Eu^{2+} luminescence centers (Fig. 9c). A very low critical quenching concentration of Eu^{2+} luminescence can be explained by the significantly shorter distance of Li_{Eu}–Li_{Eu} (~2.80–2.87 Å) in $Li_{1-2x}Eu_xSi_2N_3$, in which the possibility of energy transfer exceeds that of the emission from the $5d \rightarrow 4f$ transition of Eu^{2+}. Consequently, the absorbed excitation energy is mainly migrated through the host lattice not the luminescent centers of Eu^{2+}. In addition, at higher x values, the increased Li vacancies can be regarded as the electron traps, which could be another important reason for reducing the luminescence intensity. The emission band shows a slight red shift from 572 to 584 nm with an increase in Eu concentration because of the local structure relaxation by replacing Li^+ with Eu^{2+} (see Section 3.2). This is also in agreement with the reflection spectra of $Li_{1-2x}Eu_xSi_2N_3$ (Fig. 9d), in which the absorption edge of Eu^{2+} gradually shifts to longer wavelengths with increasing Eu^{2+} concentration, evidently indicating that the Eu^{2+} ions can be incorporated into the $LiSi_2N_3$ lattice.

Low luminescence intensity of Eu^{2+} in $LiSi_2N_3$ is mainly caused by the photoionization process, which the excited $5d$ electrons of Eu^{2+} have high opportunities within the conduction band and can recombine nonradiatively with the positive holes most likely at the Li^+ site. This is strongly supported by the fact that largely overlapping of the host lattice excitation band with the top of the $5d$ excitation band of Eu^{2+}, as shown in Fig. 9b.

Fig. 10 shows the temperature dependence of $Li_{1-2x}Eu_xSi_2N_3$ ($x = 0.002$). The thermal quenching rate of Eu^{2+} is markedly high and the relative emission intensity shows a nearly parabolic decrease with rising temperature even for lower Eu^{2+} concentrations. The observed thermal quenching temperature (T_{50}, at which its relative intensity is half of the initial intensity at room temperature) is about 96 °C for $Li_{1-2x}Eu_xSi_2N_3$ ($x = 0.002$). Clearly, the degradation rate of the Eu^{2+} emission at about 580 nm is higher than that of the shoulder originating from band-to-band transition at about 480 nm against temperature. When the temperature is above 100 °C, the dominant emission maximum
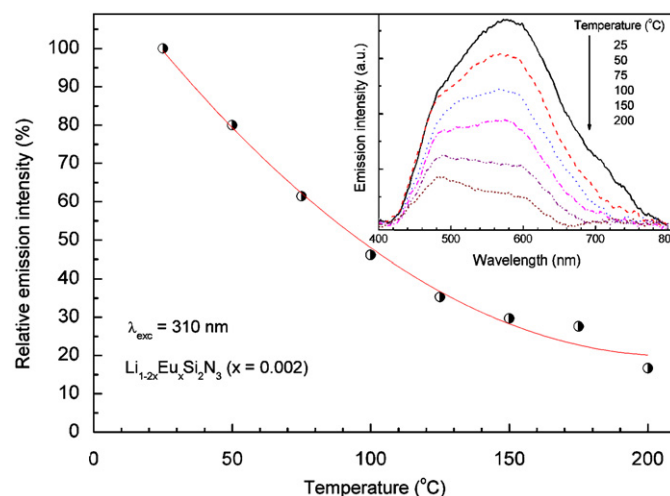

Fig. 10. Temperature dependence of $Li_{1-2x}Eu_xSi_2N_3$ ($x = 0.002$) under excitation at 310 nm.

has been exchanged from 580 to 480 nm. In addition, the emission band of Eu^{2+} exhibits a slight blue shift, while the position of the emission shoulder at 480 nm is nearly unchangeable with increasing temperature (see inset in Fig. 10), which indirectly confirms that the emission shoulder at 480 nm does not belong to the $4f^6 5d \rightarrow 4f^7$ transition of Eu^{2+}. It is believed that thermal ionization is mainly responsible for quenching of the luminescence of Eu^{2+} at high temperatures [11], because the excited 5d electrons are easily ionized by the absorption of thermal energy and entrance into the bottom of the conduction band of the host through the top of the Eu^{2+} excitation levels. As the energy gap from the valence to conduction bands is much larger than that of the top of the 5d levels of Eu^{2+} to the conduction band, the excited 5d electrons of Eu^{2+} are easily promoted to the conduction band and subsequently are ionized. As a result, the thermal quenching rate of Eu^{2+} luminescence is higher than that of the electron transition from the conduction to valence bands.

To further improve and modify the luminescence properties of $LiSi_2N_3:Eu^{2+}$, double substitution on the metal and nonmetal cation sites has been found to be more effective than that on the nonmetal and anion sites (i.e. Al–Si, O–N). Fig. 11 shows the excitation and emission spectra of the modified $LiSi_2N_3:Eu^{2+}$ by two substitutional ways. It can be seen that the profiles of the emission band have been markedly changed and the luminescence intensity have been increased compared with $Li_{1-2x}Eu_xSi_2N_3$ ($x = 0.01$). With respect to $Li_{1-2x}Eu_xSi_{2-y}Al_yN_{3-y}O_y$ ($x = 0.01$, $y = 0.04$), the emission shoulder at about 480 nm is significantly enhanced and already becomes the dominant band (Fig. 11a), which probably can be explained by the band gap narrowing between the valence and conduction bands of the $LiSi_2N_3$ host due to the substitution $(AlO)^+$ for $(SiN)^+$, similar to the findings in the Sialon materials [46–48]. However, the shift of the Eu^{2+} emission band is very limited for the incorporation of

$(AlO)^+$. In contrast, the replacement of $(LiSi)^{5+}$ with $(CaAl)^{5+}$ results in a large red shift of the emission band for $Li_{1-2x-y}Ca_yEu_xSi_{2-y}Al_yN_3$. In addition to an extension of the emission band from yellow ($\sim$580 nm) to red spectral region ($\sim$620 nm), the luminescence intensity is significantly increased (Fig. 11b), showing high potential for white LED applications, especially for use in white UV–LEDs. As there are no obvious changes for the observed excitation spectra, implying very limited changes in the crystal field splitting (CFG) and the center of gravity (COG) of the 5d excitation states of Eu^{2+}, the red shift of the emission band can be mainly attributed to the Stokes shift arising from the large structural relaxation as mentioned in Section 3.2.

3.3.2. $LiSi_2N_3:Ce^{3+}$

Fig. 12a shows the excitation and emission spectra of $Li_{1-3x}Ce_xSi_2N_3$ ($x = 0.005$) as well as the decomposed excitation spectrum. The excitation band of Ce^{3+} narrowly ranges from 230–400 nm and is composed of four Gaussian bands at about 253, 284, 313 and 344 nm, in which the top of the first two excitation bands, e.g., 253 and 284 nm, are large overlap with the host excitation band of $LiSi_2N_3$ in UV range of 200–270 nm (Fig. 12b). In comparison with $Li_{1-2x}Eu_xSi_2N_3$, the band-to-band excitation from the host is much stronger than the 5d excitation of Ce^{3+}, which must be related to stronger interaction between Ce–Ce because of a significantly short Li_{Ce}–Li_{Ce} distance (2.826(14) Å). This strong band-to-band excitation of the host can be explained by the fact that the absorbed energy of the host lattice prefers to migrate by the conduction to valence bands
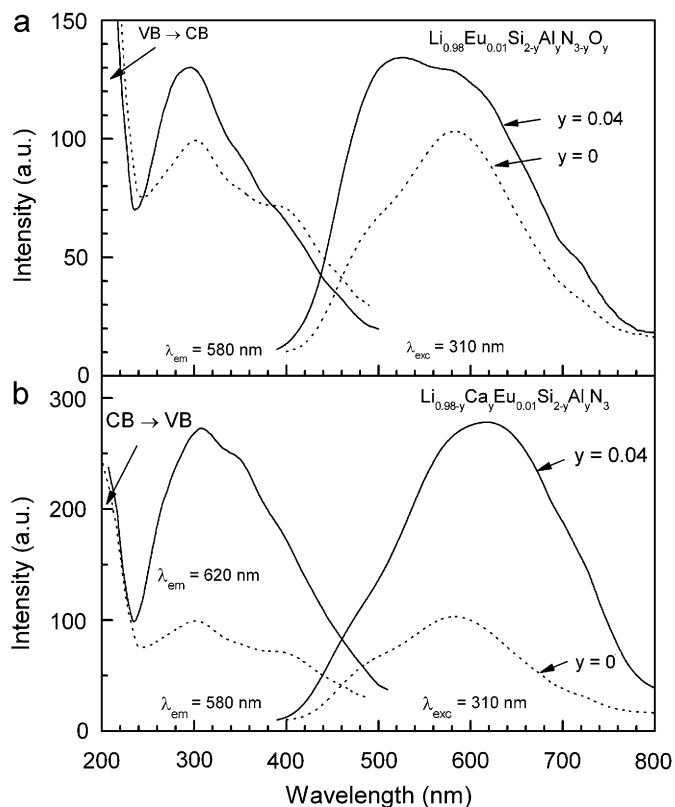

Fig. 11. Excitation and emission spectra of (a) $Li_{1-2x}Si_{2-y}Al_yN_{3-y}O_y$ ($x = 0.01$ and $y = 0.04$), and (b) $Li_{1-2x-y}Ca_yEu_xSi_{2-y}Al_yN_3$ ($x = 0.01$ and $y = 0.04$).
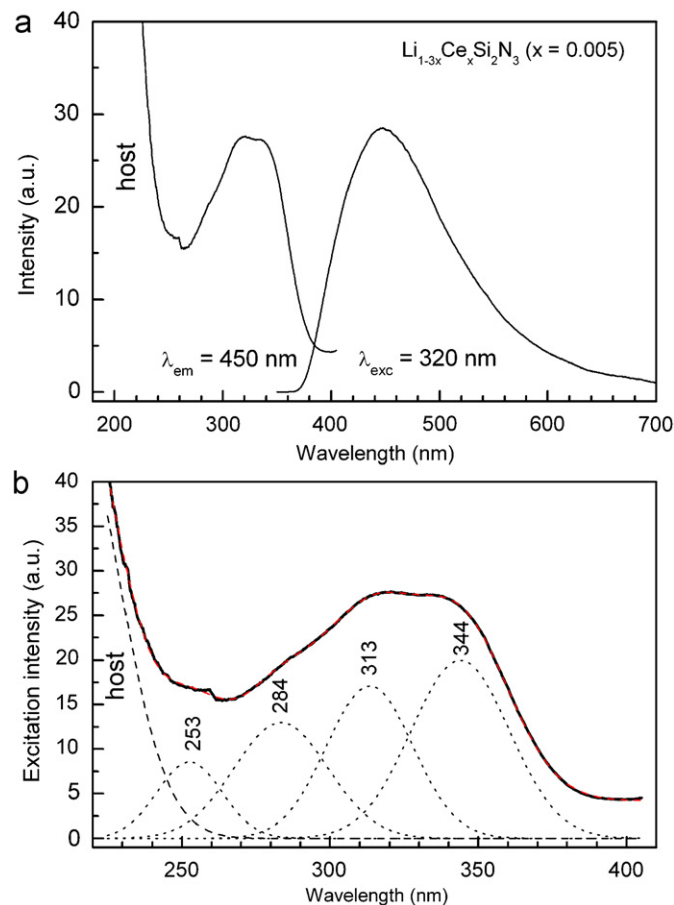
Fig. 12. Excitation and emission spectra as well as the decomposed excitation spectrum of $Li_{1-3x}Ce_xSi_2N_3$ ($x = 0.005$).

transition since the lowest $5d$ excitation band of Ce^{3+} is located at lower energies than that of Eu^{2+} in between the valence and conduction bands, which provides high possibility for the band-to-band transition of the 2p and 3p electrons of Li and N, respectively. Therefore, the emission band centered at about 450 nm originating from the $5d\rightarrow 4f$ transition of Ce^{3+} is remarkably overlapping with the emission band centered at about 480 nm arising from the electron transition between the conduction to valence bands. Exactly like in the case of $Li_{1-2x}Eu_xSi_2N_3$, the absorbed energy by the host cannot be efficiently transferred to the activator of the Ce^{3+} ions. Additionally, as the top of the excitation states of Ce^{3+} already lie in the bottom of the conduction band, photoionization process is a main reason for lower luminescence intensity of Ce^{3+}. Of course, the Li vacancies formed by the substitution Ce^{3+} for Li^+, which results in a number of luminescence killers in the $LiSi_2N_3$ host, is also an important reason. Furthermore, an unusual short distance of Li_{Ce}–Li_{Ce} certainly will lead to self quenching between the Ce^{3+} ions.

3.3.3. $LiSi_2N_3:Tb^{3+}$

In contrast to the $4f\leftrightarrow 5d$ transitions of Eu^{2+} and Ce^{3+}, the $4f^8\leftrightarrow 4f^75d$ transitions of Tb^{3+} within the f-shell are the dominant luminescence processes, which is almost independent of the local environment. Fig. 13 shows the excitation and emission spectra of $Li_{1-3x}Tb_xSi_2N_{2.994167}O_{0.00875}$ ($x = 0.005$). As usual, the excitation band of Tb^{3+} is positioned at higher energy levels than that of Eu^{2+} or Ce^{3+} (see Figs. 9 and 12) ranging from 200 to 280 nm peaking at about 236 nm. As the major excitation states of Tb^{3+} are just below and/or partially overlapping with the conduction band of the host, the electrons such as Li 2p electrons within the upper part of the valence bands can hardly cross over the energy gap ($\geqslant 5.0$ eV) to the conduction bands without the lower-lying $5d$ levels of Eu^{2+} or Ce^{3+} in relays during the excitation processes. Therefore, the band-to-band excitation attributed to the electron transition from the valence to conduction bands is much weaker than the f-d excitation band of Tb^{3+} arising from the $4f^8\rightarrow 4f^75d^1$ transition. On the other hand, the absorption of the host and Tb^{3+} is nearly in the same spectral range that implies efficient energy transfer from the host to the Tb^{3+} ion could be realized. As a result, $LiSi_2N_3:Tb^{3+}$ gives highly efficient luminescence excited by UV light. Besides the dominant $4f^8\rightarrow 4f^75d^1$ excitation band of Tb^{3+}, the number of

the f–f excitation peaks in the visible range are very weak, as shown in an enlarged inset in Fig. 13. A comparison is made with Ce^{3+} doped $LiSi_2N_3$ which demonstrates that the energy difference between the lowest $5d$ excitation band of Ce^{3+} and the f–d excitation band of Tb^{3+} in $LiSi_2N_3$ is about $13\,300\,cm^{-1}$ exactly falling in the range of $11\,000$–$15\,000\,cm^{-1}$, as found in a large number of Tb^{3+} and Ce^{3+} doped isomorphic compounds [11]. Excitation under UV, $LiSi_2N_3:Tb^{3+}$ solely gives the set of green emission from $^5D_4\rightarrow {}^7F_J$ ($J = 3$–6) with a maximum emission peak at about 542 nm originating from the $^5D_4\rightarrow {}^7F_5$ transition of Tb^{3+}. On the one hand the nearest distance of Li_{Tb}–Li_{Tb} (2.853(16) Å) is also remarkably short which can be regarded as a highly concentrated system of Tb^{3+}, therefore, the higher-lying blue emission of $^5D_3\rightarrow {}^7F_J$ is totally quenched in a way of the cross-relaxation [11] at significantly lower Tb^{3+} concentrations in $LiSi_2N_3$, offering only green emission of Tb^{3+}

In summary, the excited $5d$ orbitals of Eu^{2+} or Ce^{3+} are compressed together with largely overlapping when it is incorporated into a small crystallographic site of Li and the most favorable excitation energy levels (excitation bands) tend to lie at high energy for Eu^{2+} or Ce^{3+}. Accordingly, it would easily result in photoionization. However, a small crystallographic site with a short-nearest distance of Li_{Tb}–Li_{Tb} is rather favorable for obtaining efficient green line emission of Tb^{3+}, by which the unwanted blue emission at higher energies can be easily quenched with significantly low Tb^{3+} concentration in $LiSi_2N_3$.

4. Conclusions

(1) $LiSi_2N_3$ is calculated to be an insulator with an indirect band gap of about 5.0 eV in fair good agreement with the experimental value of 6.4 eV. The top of the valence band is within Γ–Z which is mainly consisted of N 2p and Li 2p states, and the bottom of the conduction band is at Γ which is mainly composed of Si 3s, 3p and Li 2p states.

(2) $LiSi_2N_3$ can form limited solid solutions with the rare-earth ions of Eu^{2+}, Ce^{3+} and Tb^{3+} and the solubility of Eu^{2+} is significantly greater than that of Ce^{3+} and Tb^{3+}. $LiSi_2N_3:Eu^{2+}$ shows yellow emission at about 580 nm under UV excitation ($\lambda_{exc} = 310$ nm). The critical quenching concentration of Eu^{2+} is at about $x = 0.005$ and the thermal quenching temperature (T_{50}) is about 96 °C for $Li_{1-2x}Eu_xSi_2N_3$. By partial replacement of $(SiN)^+$ with $(AlO)^+$ as well as $(LiSi)^{5+}$ with $(CaAl)^{5+}$, the luminescence intensity can be increased, especially for the latter. In addition, the emission band of Eu^{2+} is significantly shifted from yellow (~ 580 nm) to red (~ 620 nm) by the double substitution $Ca^{2+}\rightarrow Li^+$ and $Al^{3+}\rightarrow Si^{4+}$ simultaneously in $Li_{1-2x}Eu_xSi_2N_3$, which provides opportunities as a red conversion phosphor for white LED applications. $LiSi_2N_3:Ce^{3+}$ shows blue emission with a broad band peaking at 450 nm when excited at 320 nm. The fundamental host emission (~ 480 nm) are observed for both Eu^{2+} and Ce^{3+}-doped $LiSi_2N_3$ due to the dominant electron transitions between the valence and conduction bands of the host with the aid of the lower-lying $5d$ excitation levels of Eu^{2+} and Ce^{3+} in between.

(3) $LiSi_2N_3:Tb^{3+}$ exhibits strong green line emission arising from the transition of $^5D_4\rightarrow {}^7F_J$ ($J = 3$–6) excited under UV. Due to significantly short distance of Li_{Tb}–Li_{Tb}, blue line emission from the $^5D_3\rightarrow {}^7F_J$ completely disappears even at significantly low Tb^{3+} concentration by the cross relaxation process. Unlike Eu^{2+} and Ce^{3+} doped $LiSi_2N_3$, without the lower-lying $5d$ levels, efficiently energy transfer from the host to the luminescence center of Tb^{3+} can be realized in $LiSi_2N_3$, which plays an important role for highly efficient Tb^{3+} luminescence.
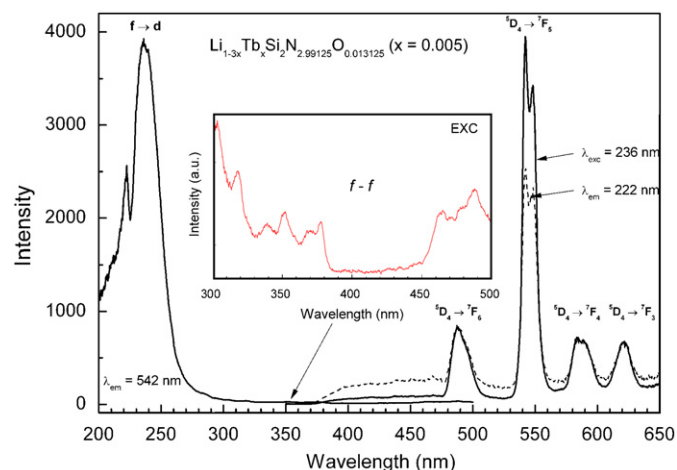

Fig. 13. Excitation and emission spectra of $Li_{1-3x}Tb_xSi_2N_{2.994167}O_{0.00875}$ ($x = 0.005$). Inset shows the enlarged f–f transition peaks of Tb^{3+} in the excitation spectrum.

Acknowledgment

References

[1] R. Mueller-Mach, G. Mueller, M.R. Krames, H.A. Höppe, F. Stadler, W. Schnick, T. Juestel, P. Schmidt, Phys. Status Solidi A 202 (2005) 1727.
[2] R.J. Xie, N. Hirosaki, M. Mitomo, in: W. Yen, S. Shionoya, H. Yamamoto (Eds.), Phosphor Handbook, second ed., CRC Press, Boca Raton, London, New York, 2007, pp. 331–338 (Chapter 3).
[3] H.A. Höppe, H. Lutz, P. Morys, W. Schnick, A. Seilmeier, J. Phys. Chem. Solids 61 (2000) 2001.
[4] Y.Q. Li, J.E.J. van Steen, J.W.H. van Krevel, G. Botty, A.C.A. Delsing, F.J. DiSalvo, G. de With, H.T. Hintzen, J. Alloys Comp. 417 (2006) 273.
[5] Y.Q. Li, G. de With, H.T. Hintzen, J. Lumin. 116 (2006) 107.
[6] Y.Q. Li, A.C.A. Delsing, G. de With, H.T. Hintzen, Chem. Mater. 17 (2005) 3242.
[7] K. Uheda, N. Hirosaki, Y. Yamamoto, A. Naito, T. Nakajima, H. Yamamoto, Electrochem. Solid State Lett. 9 (2006) 4.
[8] K. Uheda, N. Hirosaki, Y. Yamamoto, Phys. Status Solidi A 203 (2006) 2712.
[9] R.J. Xie, M. Mitomo, K. Uheda, F.F. Xu, Y. Akimune, J. Am. Ceram. Soc. 85 (2002) 1229.
[10] J.W.H. van Krevel, J.W.T. van Rutten, H. Mandal, H.T. Hintzen, R. Metselaar, J. Solid State Chem. 165 (2002) 19.
[11] G. Blasse, B.C. Grabmaier, Luminescent Materials, Springer, Berlin, 1994.
[12] J.W.H. van Krevel, H.T. Hintzen, R. Metselaar, A. Meijerink, J. Alloys Comp. 268 (1998) 272.
[13] R.J. Xie, N. Hirosaki, M. Mitomo, K. Takahashi, K. Sakuma, Appl. Phys. Lett. 88 (2006) 101104.
[14] N. Hirosaki, X.J. Xie, K. Kimoto, T. Sekiguchi, Y. Yamamoto, T. Suehiro, M. Mitomo, Appl. Phys. Lett. 86 (2005) 211905.
[15] R.J. Xie, N. Hirosaki, H.L. Li, M. Mitomo, J. Electrochem. Soc. 154 (2007) J314.
[16] J. Lang, J.P. Charlot, Rev. Chim. Miner. 7 (1970) 121.
[17] E.D. Whitney, R.F. Giese Jr., Inorg. Chem. 10 (1971) 1090.
[18] J. David, Y. Laurent, J.P. Charlot, J. Lang, Bull. Soc. Fr. Mineral. Cristallogr. 96 (1973) 21.
[19] H. Yamane, S. Kikkawa, M. Koizumi, Solid State Ionics 25 (1987) 183.
[20] M. Orth, W. Schnick, Z. Anorg, Allg. Chem. 625 (1999) 1426.
[21] R. Juza, H.H. Weber, E. Meyer-Simon, Z. Anorg. Allg. Chem. 273 (1953) 48.
[22] A.J. Anderson, R.G. Blair, S.M. Hick, R.B. Kaner, J. Mater. Chem. 16 (2006) 1318.
[23] M.S. Bhamra, D.J. Fray, J. Mater. Sci. 30 (1995) 5381.
[24] A.T. Dadd, P. Hubberstey, J. Chem. Soc. Dalton Trans. (1982) 2175.
[25] V. Ischenko, L. Kienle, M. Jansen, J. Mater. Sci. 37 (2002) 5305.
[26] S.M. Hick, C.N. Tran, R.G. Blair, R.B. Kaner, in: The 229th National Meeting of the American Chemical Society, San Diego, 2005, INOR, p. 587.
[27] A.C. Larson, R.B. Von Dreele, Report LAUR 86-748, National Laboratory, Los Alamos, NM, 2000.
[28] B.H. Toby, J. Appl. Cryst. 34 (2001) 210.
[29] V. Milman, B. Winkler, J.A. White, J. Pickard, M.C. Payne, E.V. Akhmatskaya, R.H. Nobes, Int. J. Quantum Chem. 77 (2000) 895.
[30] G. Kresse, J. Hafner, Phys. Rev. B 47 (1993) 558;
G. Kresse, J. Hafner, Phys. Rev. B 49 (1994) 14251.
[31] G. Kresse, J. Furthmuller, Comput Mater. Sci. 6 (1996) 15.
[32] G. Kresse, J. Furthmuller, Phys. Rev. B 54 (1996) 11169.
[33] J.P. Perdew, J.A. Chevary, S.H. Vosko, K.A. Jackson, M.R. Pederson, D.J. Singh, C. Fiolhais, Phys. Rev. B. 46 (1992) 6671.
[34] R. Dronskowski, P.E. Blochl, J. Chem. Phys. 97 (1993) 8617.
[35] O.K. Andersen, O. Jepsen, Phys. Rev. Lett. 53 (1984) 2571;
O.K. Andersen, Phys. Rev. B 12 (1975) 3060;
G. Krier, O. Jepsen, A. Burkhardt, O.K. Andersen, The Stuttgart TB-LMTO-ASA Program, Max-Planck-Institut fur Festkorper-forschung, Stuttgart, Germany, 1995.
[36] S.H. Vosko, L. Wilk, M. Nusair, Can. J. Phys. 58 (1980) 1200.
[37] Y.N. Xu, W.Y. Ching, Phys. Rev. B 51 (1995) 17379.
[38] C.M. Fang, R.A. de Groot, R.J. Bruls, H.T. Hintzen, G. de With, J. Phys Condens. Matter 11 (1999) 4833.
[39] C.M. Fang, H.T. Hintzen, G. de With, J. Alloys Comp. 336 (2002) 1.
[40] C.M. Fang, H.T. Hintzen, G. de With, G.A. de Groot, J. Phys. Condens. Matter 13 (2001) 67.
[41] C.M. Fang, H.T. Hintzen, G.A. de Groot, G. de With, J. Alloys Comp. 322 (2001) L1.
[42] R.D. Shannon, Acta Cryst. A 32 (1976) 751.
[43] T. Balic Zunic, I. Vickovic, J. Appl. Cryst. 29 (1996) 305.
[44] N.E. Brese, M. O'Keeffe, Acta Cryst. B 47 (1991) 192.
[45] G. Petzow, M. Herrmann, in: M. Jansen (Ed.), High Performance Non-Oxide Ceramics II (Structure and Bonding Series 102), vol. 2, Springer, Berlin, 2002, pp. 47–168.
[46] W.Y. Ching, M.Z. Huang, S.D. Mo, J. Am. Ceram. Soc. 83 (2000) 780.
[47] K. Tatsumi, I. Tanaka, H. Adachi, M. Yoshiya, Phys. Rev. B. 66 (2002) 165210.
[48] N. Hirosaki, C. Kocer, S. Ogata, K. Tatsumi, Phys. Rev. B. 71 (2005) 104105.